# Trichostatin A-induced histone acetylation causes decondensation of interphase chromatin

Katalin Fejes Tóth[1,2], Tobias A. Knoch[1,3], Malte Wachsmuth[1], Monika Frank-Stöhr[4], Michael Stöhr[4], Christian P. Bacher[5], Gabriele Müller[6] and Karsten Rippe[1,2,*]

[1]Kirchhoff-Institut für Physik, AG Molekulare Biophysik, Ruprecht-Karls-Universität Heidelberg, Im Neuenheimer Feld 227, 69120 Heidelberg, Germany
[2]Molekulare Genetik, [3]Biomedizinische Strukturanalyse, [4]Cytometrie, [5]Intelligente Bioinformatiksysteme and [6]Genregulation und DNA-Topologie, Deutsches Krebsforschungszentrum, Im Neuenheimer Feld 280, 69120 Heidelberg, Germany
*Author for correspondence (e-mail: karsten.rippe@kip.uni-heidelberg.de)

## Summary

The effect of trichostatin A (TSA)-induced histone acetylation on the interphase chromatin structure was visualized in vivo with a HeLa cell line stably expressing histone H2A, which was fused to enhanced yellow fluorescent protein. The globally increased histone acetylation caused a reversible decondensation of dense chromatin regions and led to a more homogeneous distribution. These structural changes were quantified by image correlation spectroscopy and by spatially resolved scaling analysis. The image analysis revealed that a chromatin reorganization on a length scale from 200 nm to >1 μm was induced consistent with the opening of condensed chromatin domains containing several Mb of DNA. The observed conformation changes could be assigned to the folding of chromatin during G1 phase by characterizing the effect of TSA on cell cycle progression and developing a protocol that allowed the identification of G1 phase cells on microscope coverslips. An analysis by flow cytometry showed that the addition of TSA led to a significant arrest of cells in S phase and induced apoptosis. The concentration dependence of both processes was studied.

Key words: TSA, Histone deacetylase, Image correlation spectroscopy, Fractal dimension, Cell cycle

## Introduction

The reversible (de)acetylation of the N-terminal histone tails by specific histone acetylases and deacetylases (HDAC) is involved in the regulation of gene expression. A correlation of histone acetylation with enhanced transcription was described 40 years ago (Allfrey et al., 1964). For a number of genes, a direct connection with gene expression has been demonstrated (Coffee et al., 1999; Dressel et al., 2000; Grunstein, 1997; Kouzarides, 1999; Richon et al., 2000; Sambucetti et al., 1999), and dysfunction of histone acetylases and HDACs has been associated with different types of cancer (Archer and Hodin, 1999; Cress and Seto, 2000; Kouzarides, 1999; Mahlknecht et al., 2000). Various HDAC inhibitors (HDACi) have been described that induce cell cycle arrest, differentiation, and apoptosis in cell lines. Many of these have potent antitumor activities in vivo (reviewed by Marks et al., 2001; Marks et al., 2000). One of the most effective and best studied HDAC inhibitor is trichostatin A (TSA) (Yoshida et al., 1995; Yoshida et al., 1990). A crystallographic analysis of TSA and a histone deacetylase homologue indicates that TSA interacts reversibly with the HDAC catalytic site preventing binding of the substrate (Finnin et al., 1999; Marks et al., 2001; Marks et al., 2000).

It is widely accepted that histone acetylation is essential to establish a transcriptionally competent state of chromatin (Kadonaga, 1998; Strahl and Allis, 2000; Tse et al., 1998; Zhang et al., 1998). However, the relation between chromatin conformation and histone acetylation is complex and three different effects could be important (Hansen, 2002; Hansen et al., 1998). (1) Acetylation might modulate interactions between histone tails and the DNA. Nonacetylated histone tails carry a large number of positively charged lysine and arginine residues (≈100 per nucleosome) that interact with the negatively charged phosphate groups of the DNA backbone in vitro (Allan et al., 1982; Fletcher and Hansen, 1995; Hansen, 2002; Hansen et al., 1998; van Holde, 1989). However, these electrostatic interactions are highly dependent on ion concentration, and it has been shown that core histone N-termini do not bind stably to DNA at physiological ionic strength (Fletcher and Hansen, 1995; Lee and Hayes, 1998; Usachenko et al., 1994). (2) The histone tails could affect internucleosomal association (Hansen, 2002; Hansen et al., 1998; Luger and Richmond, 1998). An interaction between the positive N-terminal H4 tail and a highly negative region on the exposed H2A-H2B surface has been identified in the crystal structure of the nucleosome (Luger et al., 1997). Again, acetylation of the corresponding lysine residues is likely to weaken this interaction. (3) The histone tail acetylation might also serve as a marker for the binding of other chromosomal proteins that subsequently induce a more open and transcriptionally competent conformation. Binding to histone tails has been described for a number of proteins like NURF, SWI/SNF and RSC (Georgel et al., 1997; Logie et al., 1999), Bdf1 (Ladurner et al., 2003) and NAP-1 (McQuibban et al.,

1998). Furthermore, the acetylation state of histone tails seems to influence both the binding of histone variants (Alvelo-Ceron et al., 2000; Waterborg and Kapros, 2002) and of linker histones (Zlatanova et al., 2000).

In vitro studies of chromatin fiber fragments by analytical ultracentrifugation and electron microscopy demonstrated that histone acetylation induced only moderate conformation changes. At approximately physiological salt concentrations but in the absence of divalent cations the sedimentation coefficient of hyperacetylated fibers was 11-15% smaller (Wang et al., 2001) and the fiber diameter was somewhat reduced (22.1±5.1 nm versus 28.1±5.8 nm) (Annunziato et al., 1988). Although it is frequently assumed or speculated that histone acetylation affects chromatin structure in vivo to create a more 'open' chromatin conformation, direct evidence for this concept is missing. Furthermore, it is currently an open question whether changes in the histone acetylation state on the nucleosome level will affect the higher order organization of the chromatin fiber. Previous in vivo studies show that upon inhibition of acetylation heterochromatin binding protein HP1 reversibly disperses within the nucleus (Maison et al., 2002). However, it is unclear whether this diffuse localization is due to weaker binding of HP1 to heterochromatic regions or if it is correlated with changes in chromatin distribution.

We have studied the effect of TSA-induced histone acetylation on the interphase chromatin conformation by confocal laser scanning microscopy (CLSM). The studies were conducted with HeLa cells stably expressing a fusion protein of histone H2A and enhanced yellow fluorescent protein (H2A-YFP). H2A-YFP is incorporated into chromatin and provides an in vivo fluorescent label that reflects the DNA density as previously demonstrated for H2B-GFP (Bestvater et al., 2002; Kanda et al., 1998; Kimura and Cook, 2001; Weidemann et al., 2003). A reversible decondensation of dense chromatin regions due to histone acetylation was detected. To quantify this effect, two advanced image analysis methods were introduced, namely image correlation spectroscopy (ICS) and spatially resolved scaling analysis (SRSA). They revealed a chromatin reorganization at the micrometer scale consistent with the opening of condensed chromatin domains over several Mb of DNA.

## Materials and Methods

### Cell culture

The HeLa cell line with autofluorescent histone H2A-YFP was constructed as described (Tobias A. Knoch, Approaching the three-dimensional organisation of the human genome, PhD thesis, Ruprecht-Karls-Universität Heidelberg, 2002). The human histone gene for H2A (GeneBank accession number 83549) was amplified by PCR and inserted into the *Eco*RI-*Bam*HI site of the promoterless plasmid pECFP-1 (Clontech). The *Hin*dIII fragment of simian virus 40 (SV40) was inserted in reverse direction into the *Hin*dIII site of the multiple cloning site of pECFP-1 and the ECFP sequence was replaced with EYFP. The resulting construct pSV-HIII-H2A-EYFP expresses a 376 amino acid fusion protein from the early SV40 promoter and consists of the human H2A gene, a seven amino acid linker and the C-terminal EYFP domain. This plasmid was introduced into HeLa (ATCC: CCL 2) cells with Lipofectamin (Life Technologies, Rockville, MD, USA) and a stable monoclonal cell line was selected with 500 µg/ml G418 (Life Technologies). The same untransfected HeLa cell line was used for control experiments and fluorescence-activated cell sorting (FACS) analysis of the cell cycle.

Cells were grown in RPMI 1640 (Life Technologies) supplemented with 10% FCS in a humidified atmosphere under 5% $CO_2$ at 37°C. Cells were allowed to attach for at least 24 hours before treatment with TSA (Sigma-Aldrich, St Louis, MO, USA).

### Western blot analysis

Treatment was conducted for 2, 6, 12 and 24 hours with final TSA concentrations of 12.5, 25, 50, 100, 200 ng/ml, respectively. Cells were washed and lysed by incubation on ice for 30 minutes in a PBS buffer supplemented with 1% NP-40, 0.5% sodium desoxycholate, 0.1% SDS and protease inhibitors. The lysate was centrifuged at >10,000 *g* and the protein concentration of the supernatant determined by ELISA (enzyme-linked immunosorbent assay) using BCA Protein Assay Reagent (Pierce, Rockford, IL, USA). Equal amounts of total protein were loaded on a 12% SDS-polyacrylamide gel, blotted, and detected with anti-GFP antibody (Abcam, Cambridge, UK) that also binds to the YFP domain and anti-lamin antibody (Santa Cruz, Santa Cruz, CA, USA).

### Flow cytometry

For FACS (fluorescence-activated cell sorting) analysis cells were incubated with 0, 50, or 100 ng/ml TSA for 12 hours or 24 hours, trypsinized and washed twice with PBS containing 0.02% (w/v) EDTA. Cells were fixed with ethanol, stored at –20°C for at least one day, and stained with a solution containing 5 µM DAPI (4,6-diamidino-2-phenylindole; Serva, Heidelberg, Germany) and 5 µM SR101 (sulforhodamine 101; Eastman Kodak, Rochester, USA) as a protein counterstain (Stoehr et al., 1976). The FACS analysis of cell cycle and apoptosis was carried out on a Cytofluorograph System 30-L (Ortho Diagnostics Systems Inc., Westwood, MA, USA) using the UV lines (351-364 nm) of an argon laser as described previously (Dean and Jett, 1974; Stoehr et al., 1976). The dependence of apoptosis on the concentration of TSA was analyzed by assuming that the percentage of cells in apoptosis ($a$) goes linear with the fractional saturation ($\theta$) of HDACs with TSA according to Eqn 1. The baseline ($b$) corresponds to the percentage of apoptotic cells present in the absence of TSA and ($c$) is the proportionality constant:

$$a = c \times \theta + b \,. \tag{1}$$

The parameter $\theta$ is calculated from the binding equilibrium given by Eqn 2 with a dissociation constant $K_d$ and cooperativity factor $\alpha$:

$$\theta = \frac{[\text{TSA}]^\alpha}{K_d^\alpha + [\text{TSA}]^\alpha} \,. \tag{2}$$

For H2A-YFP fluorescence intensity measurements by flow cytometry, cells were resuspended in medium after trypsinisation and measured with a Profile I flow cytometer (Coulter Corporation, Hialeah, FL, USA). Excitation was carried out with the 488 nm line of an argon laser and emission was measured with a band pass filter at 515-535 nm.

### Fluorescence microscopy analysis

For CLSM (confocal laser scanning microscopy) cells expressing H2A-YFP were seeded on modified cell culture dishes that had an etched grid of 175 µm spacing fixed onto the bottom of the dish. Three-dimensional stack images of living cells were acquired in the presence and absence of TSA with a Leica TCS SP2 confocal laser scanning microscope (Leica Microsystems, Mannheim, Germany) using a HCXPlApo 63×1.32 oil objective lens. An Argon laser was used for excitation at 514 nm and emission was detected at 526-651 nm. For DAPI imaging excitation was carried out with a laser diode at 405 nm and emission was recorded at 420-480 nm. Images of 512×512 pixels in stacks of about 70 frames with a pixel size of

70×70×210 nm and 12 bit intensity resolution were taken with four times averaging. For in vivo imaging, cells were held in a humid incubation chamber with temperature and $CO_2$ control (PeCon, Erbach-Bach, Germany). FRAP (fluorescence recovery after photobleaching) experiments were conducted using the Leica software. Small regions of the cell nuclei were bleached at maximal intensity at 514 nm four times and postbleach images were taken every 2 seconds for 2 minutes. The intensity in an arbitrary area within the bleached region was plotted against time. The freely mobile fraction R of H2A-YFP was determined from the fluorescence in the bleached region after a plateau was reached ($F_\infty$) and the fluorescence before ($F_i$) and after ($F_0$) bleaching according to Eqn 3. The fluorescence intensity outside the bleached region decreased to approximately 80% during the postbleach observation time. This was corrected by dividing $F_\infty$ by the correction factor $\gamma$=0.8:

$$R = \frac{F_\infty/\gamma - F_0}{F_i - F_0}. \qquad (3)$$

For cell cycle analysis on coverslips, cells were fixed in 4% paraformaldehyde with 2% sucrose for 15 minutes, permeabilized with 0.5% Triton X-100 for 5 minutes, and blocked with 4% BSA/PBS for 20 minutes at room temperature. Staining was conducted with 5.0 μM DAPI, 180 mM Tris-HCl pH 7.5 and 50% (v/v) glycerol for ≥24 hours at 4°C. Images were taken with an Axiovert S100 TV wide-field fluorescence microscope (Zeiss, Jena, Germany). The image acquisition and processing was performed on about 4000 cells per coverslip with OpenLab software (Improvision, Lexington, MA, USA) in a procedure similar to that described previously (Bestvater et al., 2002). For image analysis the background was subtracted and a threshold was set to allow recognition of cell nuclei and calculation of a binary mask. Objects of a size and intensity below that of intact nuclei were disregarded. The DNA content of each nucleus was determined from the integrated DAPI intensity and plotted in a histogram to derive the cell cycle stage. The fluorescence lifetime of H2A-YFP in the absence and presence of TSA was measured as described previously (Hanley et al., 2002).

### Image segmentation

For the quantitative analysis by spatially resolved scaling analysis (SRSA) the region of the nucleus was segmented from the CLSM stacks using the image processing software Tikal developed by C. Bacher and M. Gebhard. A 3D anisotropic diffusion filter that uses an 'edge stopping' function based on Tuckey's biweight error norm was applied (Black et al., 1998). This algorithm preserves object boundaries sharper than ordinary Gaussian filters. After noise reduction by 3D anisotropic diffusion, segmentation of the cells based on a global threshold method was conducted. The outlines of nuclei were obtained by Canny edge detection on the previously segmented images (Canny, 1986). For image correlation spectroscopy the segmentation was carried out by setting a threshold after Gaussian smoothing, which resulted in a binary mask leaving the nuclei blank.

### Image correlation spectroscopy (ICS)

The typical length of spatial chromatin density fluctuations and their amplitude were determined by calculating the radial spatial autocorrelation function of pixel intensities in CLSM images. Only intensities from pixels in the nuclei were taken. Based on the two-dimensional autocorrelation function according to

$$G(\Delta x, \Delta y) = \frac{\langle I(x + \Delta x, y + \Delta y)I(x,y) \rangle}{\langle I(x,y) \rangle^2} - 1 \qquad (4)$$

[see Petersen (Petersen, 2001) for a review of ICS theory and applications] the radial correlation function $G(r)$ was computed by averaging over all displacements with $r=\sqrt{\Delta x^2 + \Delta y^2}$. The resulting spectra were fitted with Gaussian functions using Origin (OriginLab, Northampton, MA, USA). The full width at half maximum of the shortest decay was identified as the correlation length of chromatin subcompartments while the $G(0, 0)$ value from the fit was used as normalized variance of the chromatin density fluctuations.

### Spatially resolved scaling analysis (SRSA)

The local and thus spatially resolved behavior of the chromatin mass distribution in three-dimensional CLSM image stacks was investigated by computing the weighted local fractal dimension $D_f$ (Kaye, 1989; Tobias A. Knoch, Approaching the three-dimensional organisation of the human genome, PhD thesis, Ruprecht-Karls-Universität Heidelberg, 2002; Rodríguez-Iturbe and Rinaldo, 1997). $D_f$ is the exponent that related the mass or pixel intensity $M(l)$ of a cubic measurement volume to the side length $l$ of this volume:

$$M(l) \sim l^{D_f}. \qquad (5)$$

Each image stack with a pixel size of 70×70×210 nm was placed in a grid of 70×70×70 nm for isotropic spatial measurements. The intensity values were summed up for three-dimensional boxes with up to $l$=11 grid elements around all image pixels belonging to the segmented nucleus. To account for pixels in the box not belonging to the segmented volume, the total intensity in the box was weighted with the fraction of nuclear pixels. $D_f$ was calculated by linear regression for $3 \leqslant l \leqslant 11$.

## Results

### TSA cell cycle effects were dependent on concentration and incubation time

Cell cycle effects were examined by FACS analysis to determine the total DNA content per cell after DAPI staining. Thirteen independent experiments each in triplicate were averaged. Upon treatment with TSA for 12 hours a weak arrest in G1 (increase by 11.4±8.2% at 50 ng/ml TSA and 10.6±6.3% at 100 ng/ml TSA) and an arrest in the G2/M (increase by 29.7±29.2% at 50 ng/ml TSA and 59.4±28.8% at 100 ng/ml TSA) stage was observed (Fig. 1A,B). By contrast, after 24 hours incubation, TSA caused a strong arrest in S phase in a concentration-dependent manner (increase by 42.4±16.8% at 50 ng/ml TSA and 73±24% at 100 ng/ml TSA) (Fig. 1C,D). Upon longer incubation, cells continued to progress through the cell cycle indicating that TSA induced an arrest but did not block the cells at a specific cell cycle position. The HeLa control cells and the HeLa-H2A-YFP cell line were indistinguishable with respect to the effect of TSA on cell cycle progression.

### Simultaneous inhibition of different HDACs induced apoptosis

Effects of TSA on apoptosis were also analyzed by FACS using DAPI staining. The fraction of apoptotic cells was quantified at different TSA concentrations (Fig. 2). The data showed a concentration dependence with a maximal fraction of apoptotic cells of about 20% at TSA concentrations ≥200 ng/ml (660 nM). A fit of the data to a simple binding equilibrium was conducted according to Eqns 1 and 2 with α=1. In this model only one class of TSA binding sites exists and the percentage of apoptotic cells is dependent on the saturation of these sites
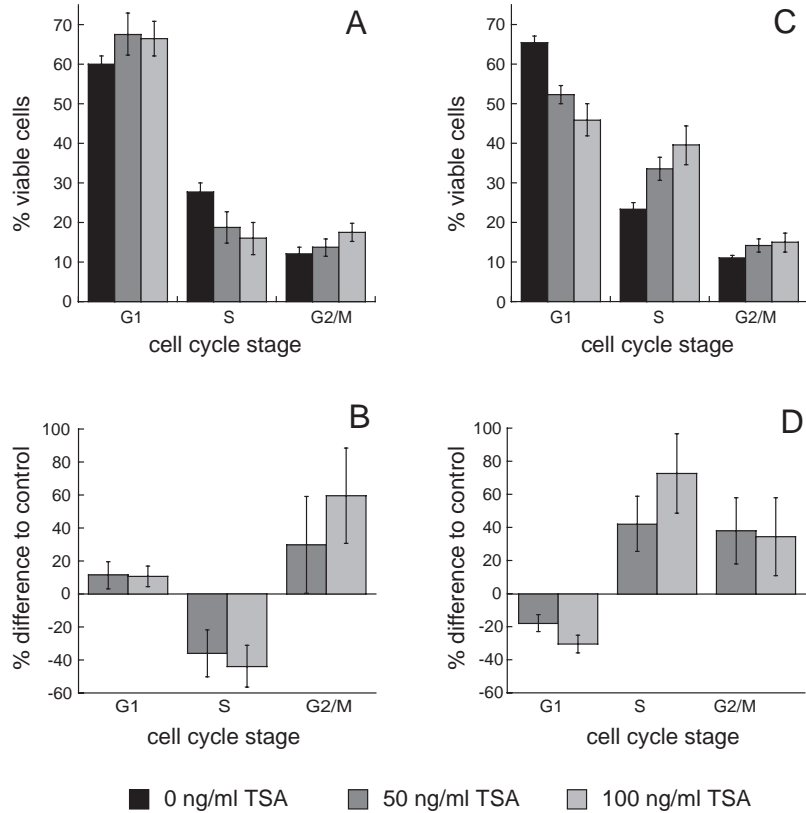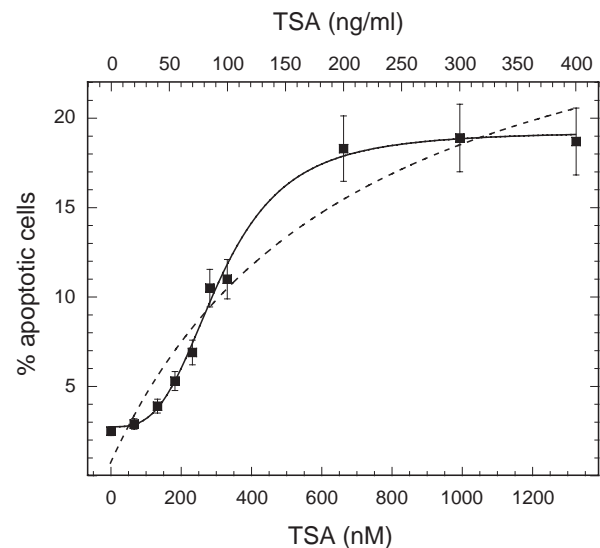
**Fig. 1.** Effect of TSA on the cell cycle as analyzed by FACS. Black bars, control cells; dark gray bars, cells treated with 50 ng/ml TSA; light gray bars, cells treated with 100 ng/ml TSA. The overall changes in the distribution after (A) 12 hours and (C) 24 hours, and the change weighted with the fraction of cells in the given cell cycle stage after (B) 12 hours and (D) 24 hours are shown.

maximum value. At a concentration of 100 ng/ml TSA, as used for imaging, a 40±3% higher fluorescence intensity was observed compared to the control cells. The differences in the cell cycle distribution for control cells (G1: 65.4±5.2%, S: 23.4±5.0%, G2/M 11.0±2.3%) and TSA-treated cells (G1: 45.9±11.0%, S: 39.5±13.6%, G2/M: 15.0±6.4%) can only partly account for this effect: assuming a DNA content of 1 $n$ (G1), 1.5 $n$ (S) and 2 $n$ (G2M) the average DNA content and fluorescence per cell would only increase by ≈10%. Measurements by in vivo fluorescence lifetime imaging experiments yielded almost identical fluorescence lifetimes of 2.92±0.18 nseconds and 2.89±0.37 nseconds in the absence and presence of TSA, respectively. Therefore, the increased fluorescence is due to a higher H2A-YFP concentration and not related to changes of the photophysical properties of the YFP-tag. Indeed, a western blot analysis showed that the total amount of H2A-YFP increased significantly (Fig. 3B). From a quantification of band intensities, a twofold increase at 100 ng/ml TSA and 24 hours incubation time is estimated. However, it should be noted that the western blot signal does

with TSA (dashed line in Fig. 2). The scaling factor $c$ in Eqn 1 accounts for the detachment of apoptotic cells from the culture dish so that a plateau value at 20% is reached. It is assumed that the probability of an apoptotic cell to detach from the dish is independent of the TSA concentration and that the time course of apoptosis is significantly shorter than the TSA incubation time of 24 hours. Furthermore, cellular uptake of TSA and equilibration to its concentration in the medium are fast on this time scale as inferred from the kinetics of TSA effects on gene expression (Mariadason et al., 2000). In Fig. 2, the fit with α=1 showed systematic deviations from the data with a value for the apparent dissociation constant of $K_d$=700 nM. If α was allowed to vary, the fit was significantly better and values of $K_d$=310 nM and α=3.2 were obtained (continuous line in Fig. 2). Thus, the concentration dependence of TSA-induced apoptosis was not simply proportional to the saturation of HDACs with TSA, but showed a rather sharp transition around a concentration of ≈300 nM (≈100 ng/μl) TSA. This behavior suggests an induction of apoptosis by TSA that would require simultaneous inhibition of three HDACs.

## TSA increased the amount of H2A-YFP incorporated into chromatin

A quantitative analysis by flow cytometry revealed that the TSA-treated cells showed an up to two-fold increase of H2A-YFP fluorescence intensity that correlated with the TSA concentration as expected for a simple binding equilibrium (Fig. 3A, Eqn 2 with α=1). The apparent dissociation constant was $K_d$=500 nM (150 ng/ml) reflecting the TSA concentration at which the fluorescence intensity reached half of the



**Fig. 2.** Concentration dependence of TSA induced apoptosis. TSA caused an increase in apoptosis in a concentration-dependent manner after incubation for 24 hours, as revealed by the FACS analysis. A fit of the data to a model in which apoptosis reflects the binding of TSA to a single class of independent binding sites (Eqn 2, α=1) showed a systematic error (dashed line). By contrast, a good fit of the data was obtained with a cooperativity factor of α=3.2 (solid line).
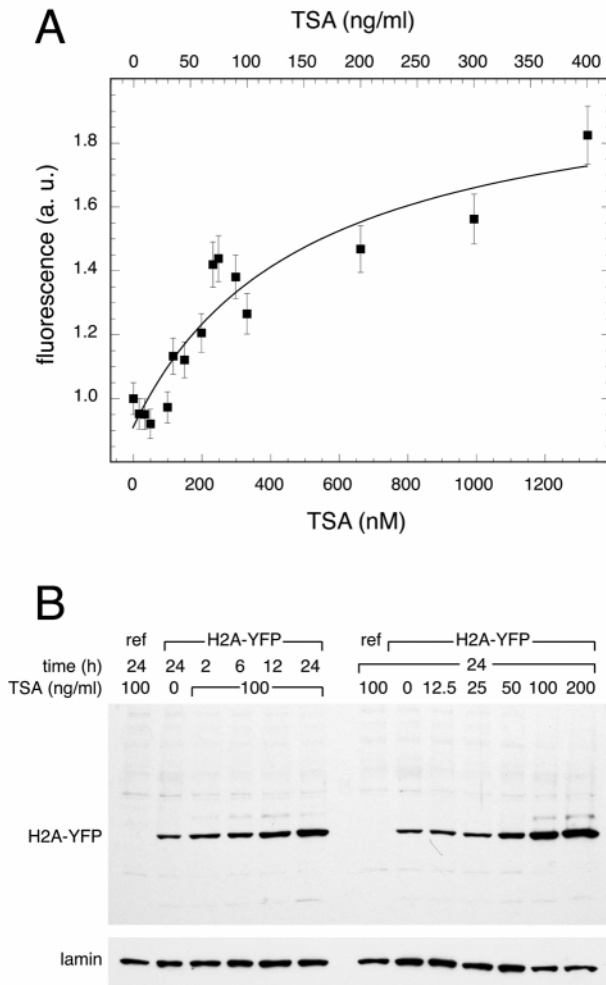
**Fig. 3.** Effects of TSA on H2A-YFP expression. (A) H2A-YFP fluorescence intensity increased upon TSA treatment. Cells were incubated with the indicated TSA concentrations for 24 hours and H2A-YFP fluorescence was measured by FACS analysis. The fluorescence intensity of untreated cells was set to 1 and the relative fluorescence increase was plotted. (B) Western blot analysis of H2A-YFP protein expression relative to that of lamin. The H2A-YFP concentration increased with longer incubation times (left) and higher TSA concentrations (right).

by CLSM to detect a reorganization of interphase chromatin. Cells were incubated with 100 ng/ml TSA for 24 hours. Under these conditions a significant increase of acetylation of histone H4 was visible on Triton-acid urea gels (data not shown) as described previously (Hoshikawa et al., 1994). The cell density was reduced to about 50%. On the CLSM images of the control cells dense chromatin regions are seen as brighter areas around the nucleolus and close to the nuclear membrane because of a higher local density of H2A-YFP. Upon TSA treatment these dense regions vanished and a more homogeneous chromatin distribution was observed (Fig. 4A,C). To confirm that the observed changes correlate with changes in the DNA distribution, DAPI images of the same cells were taken after fixation. Cells showed a somewhat altered structure probably a result of fixation but the more homogeneous distribution of DNA upon TSA treatment was still apparent (Fig. 4B,D). DAPI-stained images of control HeLa cells were also studied. In these cells TSA had a similar effect on the DNA distribution as in the H2A-YFP-expressing cells. Thus, it can be excluded that an increased incorporation of H2A-YFP (see above) caused decondensation of the chromatin.

To test whether the conformational changes induced by TSA were reversible and on which time scale they occurred, the effect of adding and removing TSA was studied (Fig. 5). After TSA addition cells were imaged every 30 minutes. Significant changes were detected after about 4 hours (Fig. 5B). Upon removal of TSA dense chromatin areas reappeared after further incubation for 4 hours (Fig. 5C). This indicates that TSA, inhibits HDACs reversibly and that chromatin recondenses again if the TSA concentration is sufficiently reduced.

### Determining the cell cycle stage on coverslips

Since the significant increase of S phase cells upon TSA treatment could obscure a comparison of the interphase chromatin conformation, a method was developed to identify the cell cycle stage of a given cell on microscopic images. Cell were grown on coverslips with an etched grid, and living cells were imaged with CLSM using H2A-YFP as a chromatin marker (Fig. 6A). Their positions on the grid were recorded for later identification and cells were fixed and stained with DAPI. Phase contrast (Fig. 6B) and DAPI (Fig. 6C) images were acquired with an inverse epifluorescence microscope. Integrated DAPI intensities per nucleus of ≈4000 cells were plotted (Fig. 6D). Then the cell cycle stage of single cells was determined from their position in the histogram. For the quantitative image analysis only cells within the full width at half maximum from the G1 peak were used.

not display a linear response to concentration and that the 40% increase in H2A-YFP fluorescence determined by FACS analysis is more reliable. The FRAP analysis of the cells revealed that TSA had no significant effect on the ratio of incorporated to free H2A-YFP. Average values for the fraction of free H2A-YFP determined according to Eqn 3 for 15 cells were 11.1±4.5% (control) and 17.1±5.9% (100 ng/ml TSA, 24 hours). Thus, the TSA-treated cells had an approximately 30% higher concentration of chromatin-incorporated H2A-YFP, when differences in the cell cycle stage distribution were taken into consideration and the concentration of H2A-YFP in the cytosol was assumed to be constant.

### TSA induced a reversible decondensation of interphase chromatin

The effect of TSA was studied with H2A-YFP-expressing cells

### Quantification of changes in chromatin morphology

The structural differences of the interphase chromatin conformation due to TSA-induced histone acetylation were quantified by image correlation spectroscopy (ICS) and by spatially resolved scaling analysis (SRSA). Both methods revealed a significant effect of increased histone acetylation on the nuclear structure and allowed a quantitative description of the interphase chromatin distribution. About 30 cells treated with TSA and 60 control cells were evaluated. The ICS analysis based on images of the YFP fluorescence from living cells (Fig. 4) yielded correlation lengths of 2.56±0.07 μm
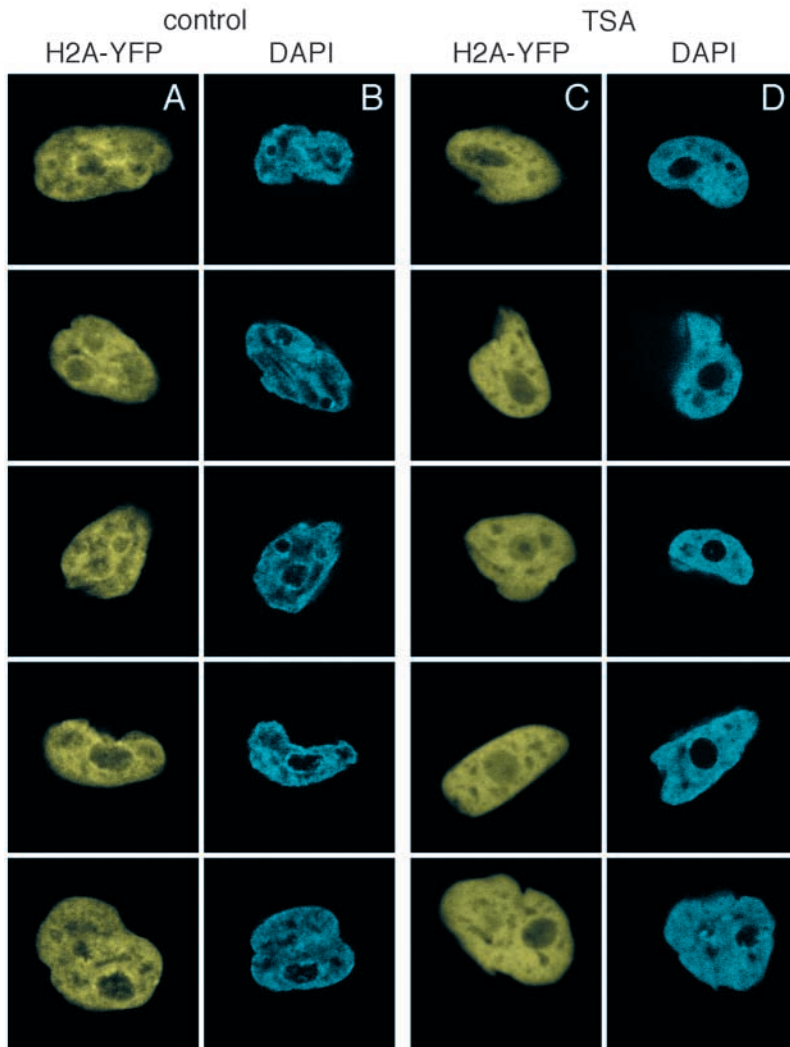
**Fig. 4.** TSA-induced changes of interphase chromatin morphology. HeLa cells stably expressing H2A-YFP were treated with 100 ng/ml TSA for 24 hours. 28 µm×28 µm (400×400 pixel) images are shown. Image intensities were normalized to the same average value. (A) Nuclei of control cells imaged in vivo with H2A-YFP. Dense chromatin areas were seen as brighter spots around the nucleolus and close to the nuclear membrane. (B) Fixed and DAPI-stained images of the same nuclei as in A. (C) TSA-treated cells imaged in vivo with H2A-YFP. The chromatin distribution was more homogeneous and most of the dense chromatin disappeared. (D) Fixed and DAPI-stained images of the same nuclei as in C.

distribution of TSA-treated cells was more similar to a homogeneously filled volume for which one would get a fractal dimension of 3. Again very similar results were obtained for the local fractal dimension when analyzing the DNA distribution in DAPI-stained images of fixed H2A-YFP cells (Fig. 4B,D). Peaks at 2.823 (+TSA) and 2.537 (control) were observed, which had widths of $\sigma=0.032$ (+TSA) and 0.071 (control).

## Discussion

### TSA affects cell cycle progression

It has been reported that TSA induces an arrest in G1 or G2/M phase (Hoshikawa et al., 1994; Inokoshi et al., 1999; Yamashita et al., 2003; Yoshida and Beppu, 1988). While a moderate arrest of cells in G1 and G2/M was observed in our experiments after an incubation time of 12 hours at 50 and 100 ng/ml, a more pronounced arrest in S phase was apparent if cells were incubated for 24 hours in the presence of the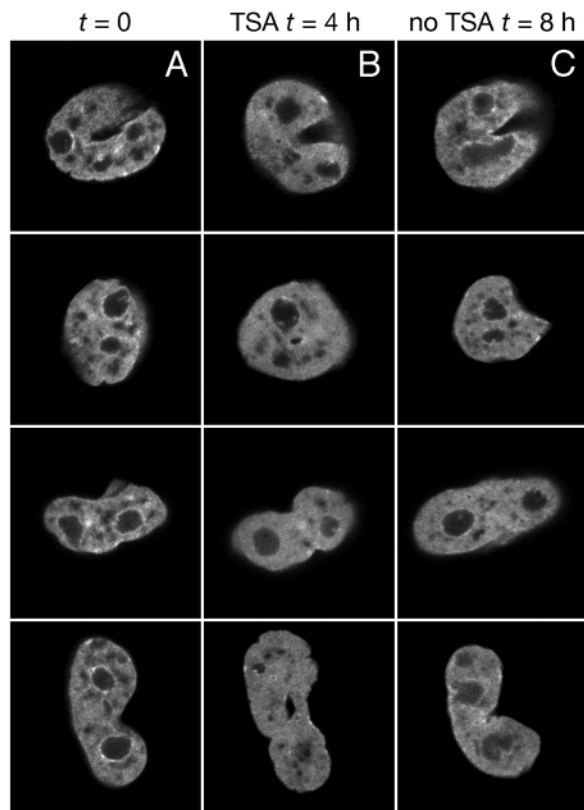 same TSA concentrations. Thus, for certain combinations of TSA concentrations and incubation times, a previously not observed strong arrest in S phase was induced. The HeLa cells studied here required about 18.5 hours to complete one cell cycle (Tobias A. Knoch, Approaching the three-dimensional organisation of the human genome, PhD thesis, Ruprecht-Karls-Universität Heidelberg, 2002), which is fast compared to other cell lines. Experiments conducted with a slower growing HeLa cell line showed no significant arrest in S phase after 24 hours (data not shown) the effect of TSA on cell cycle progression might be related to the growth rate.

The above results indicate that it was important to select cells in G1 phase for the image analysis in order to separate differences in cell cycle progression from structural changes in interphase chromatin. While the cell cycle stage can be determined by immunostaining using cell cycle-specific marker proteins, a more direct and reliable method is determining the DNA content. This was done for single cells on the coverslip by calculating the integrated DAPI intensities after fixation. It allowed the assignment of the cell cycle stage to single cells previously imaged in vivo. As compared to the FACS analysis a broadening of the distribution was observed (Fig. 3D). The differences to the FACS histograms are probably related to the potentially

(+TSA) and 1.27±0.07 µm (control) and an intensity variance of 0.045±0.004 (+TSA) and 0.055±0.003 (control) (Fig. 7). Thus, in TSA-treated cells chromatin density fluctuations on distances >1 µm were significantly longer and with a lower intensity variance, indicative of a more homogeneous distribution. This qualitative difference was also found in DAPI images of fixed H2A-YFP-expressing cells (Fig. 4B,D) with correlation lengths of 1.22±0.07 µm (+TSA) and 0.75±0.07 µm (control). The same HeLa cell line but without H2A-YFP displayed similar values of 1.49±0.07 µm (+TSA) and 0.88±0.07 µm (control) showing that decondensation did not result from the higher incorporation of H2A-YFP. The about two-fold longer correlation length obtained for the in vivo H2A-YFP images might be due to fast chromatin movements during imaging and/or artifacts induced by the fixation of cells.

On a local scale <800 nm, i.e. below the above-mentioned correlation lengths, the SRSA histograms based on images of the H2A-YFP fluorescence from living cells showed clear peaks at 2.815 (+TSA) and 2.415 (control, Fig. 8). The distributions had a standard deviation of $\sigma=0.046$ (+TSA) and 0.065 (control) around the peak when fit with a Gaussian function. The rather large differences indicate that because of decondensation of chromatin, the local chromatin density

**Fig. 5.** Reversibility of TSA-induced chromatin decondensation. CLSM images of the same cell nuclei before treatment with TSA (A), after incubation with 100 ng/ml TSA for 4 hours (B), and after changing to a medium without TSA and incubation for another 4 hours (C). The effect of TSA is reversible since dense chromatin regions reappeared after washing out TSA.

incomplete or reduced excitation of nuclear regions outside the focal plane, the fixation procedure (paraformaldehyde versus ethanol) and the different algorithm used for the analysis. Nevertheless, the method applied here allows the analysis of the cell cycle stage and the reliable identification of G1 phase cells in the microscope by a direct determination of the DNA content.

## TSA-induced apoptosis and H2A-YFP expression

Previous studies suggest that apoptosis caused by TSA treatment is preceded by histone hyperacetylation (Lee et al., 1996) and requires new protein synthesis (Medina et al., 1997). The concentration-dependent effects of TSA on apoptosis deviated significantly from a simple model, in which the number of apoptotic cells reflects the saturation of a single HDAC by TSA (Fig. 2). However, an excellent fit of the apoptosis data was obtained for a model that assumes a cooperative concentration dependence of TSA on HDAC activity. Since the structural analysis of the catalytic HDAC center shows only the reversible binding of one TSA molecule (Finnin et al., 1999) this apparent cooperativity cannot be explained by the facilitated binding of multiple TSA molecules to a single HDAC protein. Therefore, the results indicate that

induction of apoptosis requires the simultaneous inhibition of different HDACs. From the data in Fig. 2 a cooperativity factor of $\alpha=3.2$ was derived, which suggests that the simultaneous inhibition of HDAC activity at three different targets can lead to apoptosis. To date 17 human genes have been identified encoding HDACs. Eleven of these genes – members of so-called class I and II are inhibited by TSA (Johnstone, 2002). Thus, the simultaneous involvement of multiple HDACs in a complex cellular process such as apoptosis seems very possible.

In the presence of 100 ng/ml TSA the average H2A-YFP intensity per cell increased by about 40% after 24 hours (Fig. 6A) without any detectable change in the fluorescence properties as inferred from fluorescence lifetime measurements. This effect is mainly due to an increased expression of H2A-YFP protein as demonstrated by western blot analysis (Fig. 6B) and would correspond to an approximately 30% higher H2A-YFP concentration in the nucleus when accounting for differences in the cell cycle distribution. It has been shown that a number of viral promoters such as SV40, MMTV, CMV or MLP are induced by TSA up to three- to fourfold. (Dressel et al., 2000). Thus, a moderate TSA dependent induction of H2A-YFP expression is not surprising.

Within the accuracy of the measurement, the fraction of free H2A-YFP did not increase significantly as shown by FRAP experiments, indicating that the additional H2A-YFP protein is either incorporated into chromatin or that the concentration of H2A-YFP in the cytosol is increased. Since the analysis of DAPI-stained HeLa control cells without H2A-YFP showed a similar TSA-dependent decondensation as the HeLa H2A-YFP cell line, it can be excluded that the small difference in the H2A-YFP expression level contributes to the observed chromatin reorganization.

## Histone acetylation and large scale chromatin decondensation

The TSA concentration at which the HDAC activity is reduced by 50%, the $IC_{50}$ value, has been measured in vitro to be between 1.4 to 38 nM for different HDACs (Buggy et al., 2000; Furumai et al., 2001; Hoffmann et al., 2001; Yoshida et al., 1990). We have used concentrations about one order of magnitude above the $IC_{50}$ values (100 ng/ml or 330 nM TSA) to assure a significant inhibition of HDAC activity. Treatment of the cells for several hours resulted in a visible decondensation of bona fide heterochromatic areas and led to a more homogeneous distribution of chromatin. Upon removal of TSA the effect was almost completely reversed after about 4 hours. This is consistent with previous findings that TSA binds reversibly to the active center of HDACs and acts as a competitive inhibitor (Finnin et al., 1999; Yoshida et al., 1995; Yoshida et al., 1990).
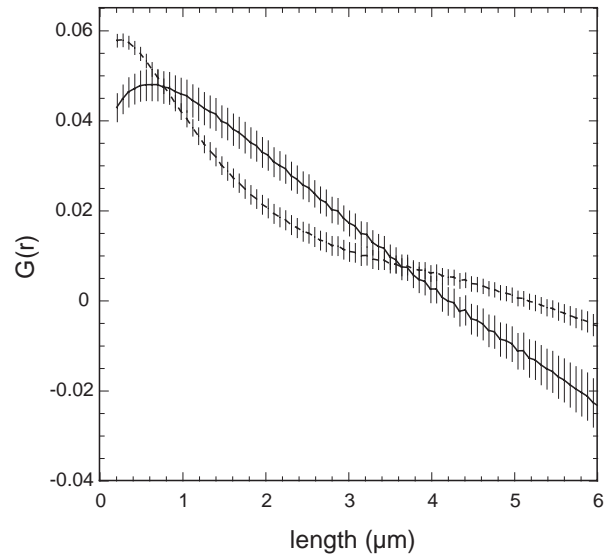
Effects of TSA on histone acetylation and gene expression have been observed within 30 minutes indicating that the uptake of TSA into the nucleus is fast on the time scale of the experiments conducted here (Mariadason et al., 2000). Previous studies demonstrated that two histone fractions exist with different kinetics of acetylation and deacetylation (Covault and Chalkley, 1980; Sun et al., 2001; Sun et al., 2003; Zhang and Nelson, 1988). About 10-15% of the histones are
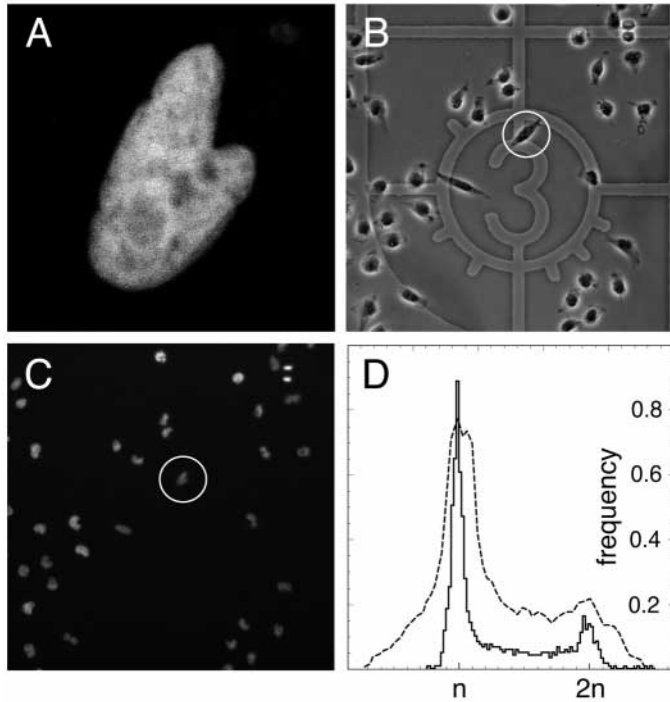
**Fig. 6.** Determination of the cell cycle stage of investigated cells. (A) In vivo CLSM images of HeLa cell nuclei expressing H2A-YFP. (B) Phase contrast image of fixed, DAPI-stained cells were taken with an inverse fluorescence microscope. The white circle shows the cell imaged in A. (C) DAPI image of the same area as in B. (D) Comparative histogram of cells analyzed by FACS (solid line) and on coverslips (dashed line). DAPI intensities of the imaged nuclei were plotted and the cell cycle stage of single cells was determined from their position in the histogram.
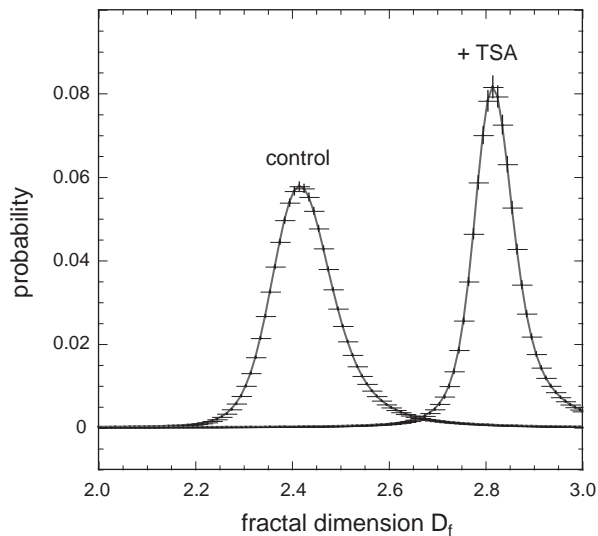


**Fig. 7.** ICS analysis of TSA-induced decondensation. Both for and The spatial radial autocorrelation function was calculated and averaged over 60 control cells ( dashed line) and 30 TSA-treated cells (solid line).

acetylated and deacetylated with a half-time ($t_{1/2}$) of about 3-8 minutes, whereas for the bulk of histones acetylation has a $t_{1/2}$ between 200 and 400 minutes, and deacetylation a $t_{1/2}$ of 30-150 minutes. From the kinetics of the reversible chromatin conformation changes observed here it appears that for complete (de)condensation the fraction of histones with a slower rate on the time scale of several hours has to be acetylated or deacetylated.

Acetylation of histone tails appears to have only moderate effects on the conformation of the 30 nm chromatin fiber in vitro and a small reduction of sedimentation coefficient and fiber diameter has been reported (Annunziato et al., 1988; Wang et al., 2001). Other more indirect effects would involve modulating the binding of chromatin-associated proteins like HP1 (Maison et al., 2002), the recruitment of chromatin remodeling complexes (Georgel et al., 1997; Logie et al., 1999) or the exchange of regular core histones with histone variants like histone H3.3, H2AX and macroH2A (Ausio et al., 2001; Hazzouri et al., 2000; Janicki et al., 2004). The chromatin reorganization described here consists of structural changes up to the μm range and must therefore reflect the three-dimensional arrangement of the chromatin fiber in the nucleus rather than its local structure. It is of interest to know whether changes in the mass density or flexibility of the 30 nm fiber would have significant effects on its higher order folding, and we are currently examining this question by computer simulations.

## Quantification of confocal images by ICS and SRSA

The ICS analysis evaluates the spatial distribution of the pixel intensity from the computation of the correlation function given in Eqn 4. In general, a specific chromatin compaction state is characterized by a non-random distribution of regions with higher and/or lower chromatin densities at certain average distances in the nucleus. This will lead to a corresponding correlation and/or anticorrelation of the intensity values, and the dimensions of given chromatin substructures can be derived from the decomposition of the correlation function in Fig. 7. The most prominent feature is the correlation length of the smallest component for which values of 2.56 μm (+ TSA) and 1.27 μm (control) were determined. Thus, on lengths above 1 μm a decondensation of chromatin upon TSA treatment was demonstrated with ICS. The correlation length of density fluctuations can be assigned to the average size of chromatin subcompartments in the order of 1.3 μm for control cells. In TSA-treated cells the length increased by a factor of two while the fluctuations showed a lower intensity variance of 0.045 as compared to 0.055 in the control. This behavior reflects the dissolution of dense chromatin domains that contain several Mb of DNA.

In the second approach introduced here for a quantitative description of the chromatin condensation state, the local fractal dimension over the whole nucleus is calculated. This method, designated as spatially resolved scaling analysis or SRSA, determines the exponent $D_f$, i.e. the fractal dimension, with which the sum of all pixel intensities increases with the side length $l$ of an observation cube around a given pixel. For a completely homogenous distribution $D_f=3$ will be obtained, since the volume of a cube increases with the third power of its length. However, if structures exist that have intensity fluctuations in the order of the length scale studied, the sum of all pixel intensities will increase with an exponent of $D_f<3$ when plotted against the length $l$ of the observation cube. Thus, by

**Fig. 8.** Spatially resolved scaling analysis (SRSA) of TSA-induced chromatin decondensation. The averaged distribution of the local fractal dimension $D_f$ was computed for both control and TSA-treated cells.

analyzing the average fractal dimension $D_f$ of the density distribution on a local scale between the optical resolution limit of 200 nm and 800 nm, the chromatin organization in general and the decondensation of chromatin after TSA treatment can be characterized. The observed increase of $D_f$ from 2.415 (control) to 2.815 (+TSA) suggests that the topology of chromatin changes significantly in the 0.2 to 0.8 µm scale with respect to loop size and/or folding pattern upon hyperacetylation (Cremer and Cremer, 2001; Tobias A. Knoch, Approaching the three-dimensional organisation of the human genome, PhD thesis, Ruprecht-Karls-Universität Heidelberg, 2002; Knoch, 2003).

ICS and SRSA clearly identify a large chromatin decondensation by TSA from averaging an ensemble of cells in G1 phase. They are complementary in the sense that the ICS analysis reveals the decondensation of chromatin subcompartments with a correlation length of 1.3 µm upon increased histone acetylation, while the SRSA results demonstrate that a more homogeneous chromatin distribution is also induced on a length scale between 0.2 to 0.8 µm. Both methods are suitable for the quantification of a wide range of structural changes not only of chromatin but also of other cellular structures. In addition, they provide an approach to quantitatively compare simulated chromatin arrangements with experimentally determined distributions from microscopic images.

## Concluding remarks

By in vivo labeling of specific chromatin loci with an autofluorescent Lac repressor it has been demonstrated that transcriptional activation is accompanied by a large-scale unfolding of chromatin (Janicki et al., 2004; Tumbar et al., 1999). It is often assumed or speculated that histone acetylation induces such an opening of chromatin. However, direct in vivo experimental support for this model has been missing. We have demonstrated here that increased histone acetylation leads to a

reversible decondensation of dense chromatin subcompartments within a range of 0.2 to >1 µm in length in living G1 phase HeLa cells. This result is consistent with the recent observation that the HDAC inhibitor suberoylanilide hydroxamic acid (SAHA) increased the DNase I sensitivity and restriction enzyme accessibility of the p21WAF1 promoter region (Gui et al., 2004).

Since the effect of acetylation per se on the conformation of the 30 nm chromatin fiber appears from in vitro studies to be moderate, it is currently an open question whether these local changes would translate into significant differences of the higher order folding of the fiber. Alternatively, acetylation might serve as a marker to recruit chromatin-remodeling complexes and/or other chromosomal proteins that change the higher order conformation of the chromatin fiber. It is anticipated that the combination of in vivo microscopy and quantitative image analysis by ICS and SRSA introduced here will prove to be useful for further studies in two aspects. First, it now becomes possible to relate high resolution images of chromatin to 3D models of the chromatin fiber folding into specific subcompartments. Second, the chromatin conformation can be reliably evaluated in cell lines in which the expression or activity of certain proteins is inhibited, for example by RNAi approaches. This would allow the in vivo identification of proteins that are essential for establishing an open chromatin structure.

## References

**Allan, J., Harborne, N., Rau, D. C. and Gould, H.** (1982). Participation of core histone "tails" in the stabilization of the chromatin solenoid. *J. Cell Biol.* **93**, 285-297.

**Allfrey, V. G., Faulkner, R. and Mirsky, A. E.** (1964). Acetylation and methylation of histones and their possible role in the regulation of RNA synthesis. *Proc. Natl. Acad. Sci. USA* **51**, 786-794.

**Alvelo-Ceron, D., Niu, L. and Collart, D. G.** (2000). Growth regulation of human variant histone genes and acetylation of the encoded proteins. *Mol. Biol. Rep.* **27**, 61-71.

**Annunziato, A. T., Frado, L. L., Seale, R. L. and Woodcock, C. L.** (1988). Treatment with sodium butyrate inhibits the complete condensation of interphase chromatin. *Chromosoma* **96**, 132-138.

**Archer, S. Y. and Hodin, R. A.** (1999). Histone acetylation and cancer. *Curr. Opin. Genet. Dev.* **9**, 171-174.

**Ausio, J., Abbott, D. W., Wang, X. and Moore, S. C.** (2001). Histone variants and histone modifications: a structural perspective. *Biochem. Cell Biol.* **79**, 693-708.

**Bestvater, F., Knoch, T. A., Langowski, J. and Spiess, E.** (2002). Construct conversions caused by simultaneous co-transfection: "GFP-walking". *Biotechniques* **32**, 848-850.

**Black, M. J., Sapiro, G., Marimont, D. H. and Heger, D.** (1998). Robust anisotropic diffusion. *IEEE Trans. Image Process.* **7**, 421-431.

**Buggy, J. J., Sideris, M. L., Mak, P., Lorimer, D. D., McIntosh, B. and Clark, J. M.** (2000). Cloning and characterization of a novel human histone deacetylase HDAC8. *Biochem. J.* **350**, 199-205.

**Canny, J. F.** (1986). A computational approach to edge detection. *IEEE Trans. Pattern Anal. Mach. Intell.* **8**, 679-698.

**Coffee, B., Zhang, F., Warren, S. T. and Reines, D.** (1999). Acetylated histones are associated with FMR1 in normal but not fragile X-syndrome cells. *Nat. Genet.* **22**, 98-101.

**Covault, J. and Chalkley, R.** (1980). The identification of distinct populations of acetylated histone. *J. Biol. Chem.* **255**, 9110-9116.

**Cremer, T. and Cremer, C.** (2001). Chromosome territories, nuclear architecture and gene regulation in mammalian cells. *Nat. Rev. Genet.* **2**, 292-301.

**Cress, W. D. and Seto, E.** (2000). Histone deacetylases, transcriptional control, and cancer. *J. Cell. Physiol.* **184**, 1-16.

**Dean, P. N. and Jett, J. H.** (1974). Mathematical analysis of DNA distributions derived from flow microfluorometry. *J. Cell Biol.* **60**, 523-527.

**Dressel, U., Renkawitz, R. and Baniahmad, A.** (2000). Promoter specific sensitivity to inhibition of histone deacetylases: implications for hormonal gene control, cellular differentiation and cancer. *Anticancer Res.* **20**, 1017-1022.

**Finnin, M. S., Donigian, J. R., Cohen, A., Richon, V. M., Rifkind, R. A., Marks, P. A., Breslow, R. and Pavletich, N. P.** (1999). Structures of a histone deacetylase homologue bound to the TSA and SAHA inhibitors. *Nature* **401**, 188-193.

**Fletcher, T. M. and Hansen, J. C.** (1995). Core histone tail domains mediate oligonucleosome folding and nucleosomal DNA organization through distinct molecular mechanisms. *J. Biol. Chem.* **270**, 25359-25362.

**Furumai, R., Komatsu, Y., Nishino, N., Khochbin, S., Yoshida, M. and Horinouchi, S.** (2001). Potent histone deacetylase inhibitors built from trichostatin A and cyclic tetrapeptide antibiotics including trapoxin. *Proc. Natl. Acad. Sci. USA* **98**, 87-92.

**Georgel, P. T., Tsukiyama, T. and Wu, C.** (1997). Role of histone tails in nucleosome remodeling by *Drosophila* NURF. *EMBO J.* **16**, 4717-4726.

**Grunstein, M.** (1997). Histone acetylation in chromatin structure and transcription. *Nature* **389**, 349-352.

**Gui, C. Y., Ngo, L., Xu, W. S., Richon, V. M. and Marks, P. A.** (2004). Histone deacetylase (HDAC) inhibitor activation of p21WAF1 involves changes in promoter-associated proteins, including HDAC1. *Proc. Natl. Acad. Sci. USA* **101**, 1241-1246.

**Hanley, Q. S., Arndt-Jovin, D. J. and Jovin, T. M.** (2002). Spectrally resolved fluorescence lifetime imaging microscopy. *Appl. Spectrosc.* **56**, 155-166.

**Hansen, J. C.** (2002). Conformational dynamics of the chromatin fiber in solution: determinants, mechanisms, and functions. *Annu. Rev. Biophys. Biomol. Struct.* **31**, 361-392.

**Hansen, J. C., Tse, C. and Wolffe, A. P.** (1998). Structure and function of the core histone N-termini: more than meets the eye. *Biochemistry* **37**, 17637-17641.

**Hazzouri, M., Pivot-Pajot, C., Faure, A. K., Usson, Y., Pelletier, R., Sele, B., Khochbin, S. and Rousseaux, S.** (2000). Regulated hyperacetylation of core histones during mouse spermatogenesis: involvement of histone deacetylases. *Eur. J. Cell Biol.* **79**, 950-960.

**Hoffmann, K., Heltweg, B. and Jung, M.** (2001). Improvement and validation of the fluorescence-based histone deacetylase assay using an internal standard. *Arch. Pharm.* **334**, 248-252.

**Hoshikawa, Y., Kwon, H. J., Yoshida, M., Horinouchi, S. and Beppu, T.** (1994). Trichostatin A induces morphological changes and gelsolin expression by inhibiting histone deacetylase in human carcinoma cell lines. *Exp. Cell Res.* **214**, 189-197.

**Inokoshi, J., Katagiri, M., Arima, S., Tanaka, H., Hayashi, M., Kim, Y. B., Furumai, R., Yoshida, M., Horinouchi, S. and Omura, S.** (1999). Neuronal differentiation of neuro 2a cells by inhibitors of cell cycle progression, trichostatin A and butyrolactone I. *Biochem. Biophys. Res. Commun.* **256**, 372-376.

**Janicki, S. M., Tsukamoto, T., Salghetti, S. E., Tansey, W. P., Sachidanandam, R., Prasanth, K. V., Ried, T., Shav-Tal, Y., Bertrand, E., Singer, R. H. et al.** (2004). From silencing to gene expression: real-time analysis in single cells. *Cell* **116**, 683-698.

**Johnstone, R. W.** (2002). Histone-deacetylase inhibitors: novel drugs for the treatment of cancer. *Nat. Rev. Drug. Discov.* **1**, 287-299.

**Kadonaga, J. T.** (1998). Eukaryotic transcription: an interlaced network of transcription factors and chromatin-modifying machines. *Cell* **92**, 307-313.

**Kanda, T., Sullivan, K. F. and Wahl, G. M.** (1998). Histone-GFP fusion protein enables sensitive analysis of chromosome dynamics in living mammalian cells. *Curr. Biol.* **8**, 377-85.

**Kaye, B. H.** (1989). *A Random Walk Through Fractal Dimensions*. New York, NY: VCH.

**Kimura, H. and Cook, P. R.** (2001). Kinetics of core histones in living human cells: little exchange of H3 and H4 and some rapid exchange of H2B. *J. Cell Biol.* **153**, 1341-1353.

**Knoch, T. A.** (2003). Towards a hollistic understanding of the human genome by determination and integration of its sequential and three-dimensional organization. In *High Performance Computing in Science and Engineering* (ed. E. Krause, W. Jäger and M. Resch), pp. 421-440. Heidelberg, Germany: Springer.

**Kouzarides, T.** (1999). Histone acetylases and deacetylases in cell proliferation. *Curr. Opin. Genet. Dev.* **9**, 40-48.

**Ladurner, A. G., Inouye, C., Jain, R. and Tjian, R.** (2003). Bromodomains mediate an acetyl-histone encoded antisilencing function at heterochromatin boundaries. *Mol. Cell* **11**, 365-376.

**Lee, K. M. and Hayes, J. J.** (1998). Linker DNA and H1-dependent reorganization of histone-DNA interactions within the nucleosome. *Biochemistry* **37**, 8622-8628.

**Lee, E., Furukubo, T., Miyabe, T., Yamauchi, A. and Kariya, K.** (1996). Involvement of histone hyperacetylation in triggering DNA fragmentation of rat thymocytes undergoing apoptosis. *FEBS Lett.* **395**, 183-187.

**Logie, C., Tse, C., Hansen, J. C. and Peterson, C. L.** (1999). The core histone N-terminal domains are required for multiple rounds of catalytic chromatin remodeling by the SWI/SNF and RSC complexes. *Biochemistry* **38**, 2514-2522.

**Luger, K. and Richmond, T. J.** (1998). DNA binding within the nucleosome core. *Curr. Opin. Struct. Biol.* **8**, 33-40.

**Luger, K., Mäder, A. W., Richmond, R. K., Sargent, D. F. and Richmond, T. J.** (1997). Crystal structure of the nucleosome core particle at 2.8 Å resolution. *Nature* **389**, 251-260.

**Mahlknecht, U., Ottmann, O. G. and Hoelzer, D.** (2000). When the band begins to play: histone acetylation caught in the crossfire of gene control. *Mol. Carcinog.* **27**, 268-271.

**Maison, C., Bailly, D., Peters, A. H., Quivy, J. P., Roche, D., Taddei, A., Lachner, M., Jenuwein, T. and Almouzni, G.** (2002). Higher-order structure in pericentric heterochromatin involves a distinct pattern of histone modification and an RNA component. *Nat. Genet.* **30**, 329-334.

**Mariadason, J. M., Corner, G. A. and Augenlicht, L. H.** (2000). Genetic reprogramming in pathways of colonic cell maturation induced by short chain fatty acids: comparison with trichostatin A, sulindac, and curcumin and implications for chemoprevention of colon cancer. *Cancer Res.* **60**, 4561-4572.

**Marks, P. A., Richon, V. M. and Rifkind, R. A.** (2000). Histone deacetylase inhibitors: inducers of differentiation or apoptosis of transformed cells. *J. Natl. Cancer Inst.* **92**, 1210-1216.

**Marks, P. A., Richon, V. M., Breslow, R. and Rifkind, R. A.** (2001). Histone deacetylase inhibitors as new cancer drugs. *Curr. Opin. Oncol.* **13**, 477-483.

**McQuibban, G. A., Commisso-Cappelli, C. N. and Lewis, P. N.** (1998). Assembly, remodeling, and histone binding capabilities of yeast nucleosome assembly protein 1. *J. Biol. Chem.* **273**, 6582-6590.

**Medina, V., Edmonds, B., Young, G. P., James, R., Appleton, S. and Zalewski, P. D.** (1997). Induction of caspase-3 protease activity and apoptosis by butyrate and trichostatin A (inhibitors of histone deacetylase): dependence on protein synthesis and synergy with a mitochondrial/cytochrome c-dependent pathway. *Cancer Res.* **57**, 3697-3707.

**Petersen, N. O.** (2001). FCS and spatial correlations on biological surfaces. In *Fluorescence Correlation Spectroscopy – Theory and Applications*, (ed. R. Rigler and E. S. Elson), pp. 162-184. Heidelberg, Germany: Springer.

**Richon, V. M., Sandhoff, T. W., Rifkind, R. A. and Marks, P. A.** (2000). Histone deacetylase inhibitor selectively induces p21WAF1 expression and gene-associated histone acetylation. *Proc. Natl. Acad. Sci. USA* **97**, 10014-10019.

**Rodríguez-Iturbe, I. and Rinaldo, A.** (1997). *Fractal River Basins – Chance and Self-organization*. Cambridge, UK: Cambridge University Press.

**Sambucetti, L. C., Fischer, D. D., Zabludoff, S., Kwon, P. O., Chamberlin, H., Trogani, N., Xu, H. and Cohen, D.** (1999). Histone deacetylase inhibition selectively alters the activity and expression of cell cycle proteins leading to specific chromatin acetylation and antiproliferative effects. *J. Biol. Chem.* **274**, 34940-34947.

**Stoehr, M., Gebhardt, U. and Goerttler, K.** (1976). Computer assistance in multiparameter flow microphotometry of mammalian cells. *Biotechnol. Bioeng.* **18**, 1057-1074.

**Strahl, B. D. and Allis, C. D.** (2000). The language of covalent histone modifications. *Nature* **403**, 41-45.

**Sun, J. M., Chen, H. Y. and Davie, J. R.** (2001). Effect of estradiol on histone acetylation dynamics in human breast cancer cells. *J. Biol. Chem.* **276**, 49435-49442.

**Sun, J. M., Spencer, V. A., Chen, H. Y., Li, L. and Davie, J. R.** (2003).

Measurement of histone acetyltransferase and histone deacetylase activities and kinetics of histone acetylation. *Methods* **31**, 12-23.

**Tse, C., Georgieva, E. I., Ruiz-Garcia, A. B., Sendra, R. and Hansen, J. C.** (1998). Gcn5p, a transcription-related histone acetyltransferase, acetylates nucleosomes and folded nucleosomal arrays in the absence of other protein subunits. *J. Biol. Chem.* **273**, 32388-32392.

**Tumbar, T., Sudlow, G. and Belmont, A. S.** (1999). Large-scale chromatin unfolding and remodeling induced by VP16 acidic activation domain. *J. Cell Biol.* **145**, 1341-1354.

**Usachenko, S. I., Bavykin, S. G., Gavin, I. M. and Bradbury, E. M.** (1994). Rearrangement of the histone H2A C-terminal domain in the nucleosome. *Proc. Natl. Acad. Sci. USA* **91**, 6845-6849.

**van Holde, K. E.** (1989). *Chromatin*. Heidelberg, Germany: Springer.

**Wang, X. Y., He, C., Moore, S. C. and Ausio, J.** (2001). Effects of histone acetylation on the solubility and folding of the chromatin fiber. *J. Biol. Chem.* **276**, 12764-12768.

**Waterborg, J. H. and Kapros, T.** (2002). Kinetic analysis of histone acetylation turnover and Trichostatin A induced hyper- and hypoacetylation in alfalfa. *Biochem. Cell Biol.* **80**, 279-293.

**Weidemann, T., Wachsmuth, M., Knoch, T. A., Müller, G., Waldeck, W. and Langowski, J.** (2003). Counting nucleosomes in living cells with a combination of fluorescence correlation spectroscopy and confocal imaging. *J. Mol. Biol.* **334**, 229-240.

**Yamashita, Y., Shimada, M., Harimoto, N., Rikimaru, T., Shirabe, K., Tanaka, S. and Sugimachi, K.** (2003). Histone deacetylase inhibitor trichostatin A induces cell-cycle arrest/apoptosis and hepatocyte differentiation in human hepatoma cells. *Int. J. Cancer* **103**, 572-576.

**Yoshida, M. and Beppu, T.** (1988). Reversible arrest of proliferation of rat 3Y1 fibroblasts in both the G1 and G2 phases by trichostatin A. *Exp. Cell Res.* **177**, 122-131.

**Yoshida, M., Kijima, M., Akita, M. and Beppu, T.** (1990). Potent and specific inhibition of mammalian histone deacetylase both in vivo and in vitro by trichostatin A. *J. Biol. Chem.* **265**, 17174-17179.

**Yoshida, M., Horinouchi, S. and Beppu, T.** (1995). Trichostatin A and trapoxin: novel chemical probes for the role of histone acetylation in chromatin structure and function. *BioEssays* **17**, 423-430.

**Zhang, D. E. and Nelson, D. A.** (1988). Histone acetylation in chicken erythrocytes. Rates of deacetylation in immature and mature red blood cells. *Biochem. J.* **250**, 241-245.

**Zhang, W., Bone, J. R., Edmondson, D. G., Turner, B. M. and Roth, S. Y.** (1998). Essential and redundant functions of histone acetylation revealed by mutation of target lysines and loss of the Gcn5p acetyltransferase. *EMBO J.* **17**, 3155-3167.

**Zlatanova, J., Caiafa, P. and van Holde, K.** (2000). Linker histone binding and displacement: versatile mechanism for transcriptional regulation. *FASEB J.* **14**, 1697-1704.